Evolution of Microstructure and Texture in Mg-Al-Zn Alloys during Electron-Beam and Gas Tungsten Arc Welding

S.H. WU, J.C. HUANG, and Y.N. WANG

The evolution of microstructure and texture in the AZ-series Mg alloys subjected to electron-beam welding and gas tungsten arc welding are examined. Electron-beam welding is demonstrated to be a promising means of welding delicate Mg plates, bars, or tubes with a thickness of up to 50 mm; gas tungsten arc welding is limited to lower-end thin Mg sheets. The grains in the fusion zone (FZ) are nearly equiaxed in shape and $\sim$8 μm or less in size, due to the rapid cooling rate. The as-welded FZ microhardness and tensile strength are higher than the base metals due to the smaller grain size. The weld efficiency, defined as the postweld microhardness or tensile strength at the mid-FZ region divided by that of the unwelded base metal, is around 110 to 125 pct for electron-beam welding and 97 to 110 pct for gas tungsten arc welding. There are three main texture components present in the electron-beam-welded (EBW) FZ, $i.e.$, $\{10\bar{1}1\}<10\bar{1}\,\bar{2}>$ (with TD//$<11\bar{2}0>$), $\{11\bar{2}1\}<1\bar{1}00>$ (with ND$_\wedge<11\bar{2}0>\sim15$ deg), and $\{10\bar{1}0\}<11\bar{2}2>$ (with WD$_\wedge<11\bar{2}0>\sim30$ deg), where TD, ND, and WD are the transverse, normal, and welding directions, respectively. The crystal growth tends to align toward the most closed-packed direction, $<11\bar{2}0>$. The texture in gas tungsten arc welded (GTAW) specimens is more diverse and complicated than the EBW counterparts, due to the limited and shallow FZ and the lower cooling rate. The cooling rates calculated by the three-dimensional (3-D) and two-dimensional (2-D) heat-transfer models are considered to be the lower and upper bounds. The cooling rate increases with decreasing Al content, increasing weld speed, and increasing distance from the weld top surface. The influences of the FZ location, welding speed, and alloy content on the resulting texture components are rationalized and discussed.

I. INTRODUCTION

MAGNESIUM alloys have been used in a wide variety of structural and nonstructural applications due to their unique properties such as low density and high special strength and elastic modulus.[1,2] They are considered as advanced materials for coping with energy-conservation and environmental-pollution regulations and are used as parts in the automobile, aircraft, or aerospace industries, where lightweight metals are needed to minimize weight or reduce internal forces at high accelerations. During the past five years, applications in automobile, bicycle, and computer, communication, and consumer electronic products have become rapidly extended.[3] Among many Mg-based alloys, the AZ- (Mg-Al-Zn), AM- (Mg-Al-Mn), and ZK- (Mg-Zn-Zr) based alloys seem to be most popular, with the AZ91 and AZ31 alloys being the lowest priced and occupying the highest market. No matter how the alloys are processed, either via the die casting or wrought route, an appropriate bonding or joining technique is crucial for their applications.

Magnesium has a high vapor pressure, low viscosity, and low surface tension, as compared with Fe-based alloys.[4] Typically, the fusion zone (FZ) of Mg alloys will be less stable, with spattering effects. A high vapor pressure will result in Mg loss during welding.[4] Also, Mg oxides and nitrides formed during welding might cause detrimental consequences. The addition of solute elements will also affect welding performance, and it was found that an Al content up to 10 wt pct aids the weldability by causing refinement of grain structure, while a Zn content of more than 1 wt pct increases hot shortness, which may cause weld cracking.[5]

There have been several welding techniques adopted for joining Mg alloys. These methods include arc welding,[6–12] friction stir welding,[13] and high-energy beam welding (laser or electron beam).[14–18] Presently, only the gas tungsten arc welding is commercially employed, mainly for the repair of cast Mg parts. For special delicate applications, laser-beam welding and electron-beam welding are also selectively applied. Electron-beam welding has long been considered to be powerful for welding thick plates, owing to its much higher FZ depth-to-width aspect ratio. On the other hand, gas tungsten arc welding would be most suitable for thin sheets, since the FZ aspect ratio is typically low. Considering the many Mg alloys that are used in the as-extruded or age-hardened condition, the gas tungsten arc welding process has some disadvantages. Due to the high energy input, a broad FZ and heat-affected zone (HAZ) are formed, necessitating a postweld heat treatment. In contrast, electron-beam welding is characterized by its excellent focusing ability, resulting in a narrow beam spot with a high energy density. This would, in turn, result in a high FZ aspect ratio, decreased HAZ dimensions, and reduction in weld distortion.[12,16]

The concentrated electron-beam energy creates a narrow and deep FZ in a thick plate due to the keyhole mechanism.[14–18] This will induce a considerably high cooling rate that would change the solidification path as compared to conventional processes such as die casting and gas tungsten arc welding, which involve slower cooling rates. Since the diffusion time and, thus, diffusion distance during electron-beam

welding are shorter, different phases may nucleate. Finer grain sizes are usually associated with faster cooling rates. Such changes may reduce the problems involved in arc welding and bring about improvement of the mechanical properties of welded parts. The typical joint efficiency (defined by the post-weld FZ hardness or strength divided by that of the unwelded base metal) for Mg alloys subjected to gas tungsten arc welding could be as high as 70 to 90 pct.[6,8] Either laser-beam or electron-beam welding of AZ-based alloys will result in a high joint efficiency of even 100 pct or higher.[12,18] For both gas tungsten arc welding and electron-beam welding, the fusion line in Mg alloys with high solute contents, such as AZ91 or AM60, was not distinct. Instead, a partially melted zone was present.[7,18]

Most studies reported in the literature on high-energy welding of Mg-based alloys were mainly centered on laser-beam welding, and only basic microstructural and mechanical properties were presented. Systemic investigations on electron-beam welding of Mg-based alloys are still very limited.[12,14–16,18] The present study is aimed at the evolution of microstructure and texture in the AZ-based plates subjected to electron-beam welding, in order to understand better the influence of high cooling rates on the microstructure and texture. Comparisons with the parallel studies on gas tungsten arc welding in the same Mg alloys are made, and the results are discussed. Texture studies of the weld zones in hexagonal Mg alloys, for the time being, are mainly for scientific curiosity, but the results might help in rationalizing the mechanical properties of the weld, as well as in understanding the grain-orientation distributions in many cast or wrought commercial Mg alloys subjected to primary or secondary thermal treatments.

II. EXPERIMENTAL METHODS

The Mg-based alloys used in this study are AZ31, AZ61, and AZ91 commercial billets purchased from the CDN Company (Delta, BC, Canada). The compositions in weight percent are listed in Table I. The Mg-based billets were machined into plates measuring 3, 30, and 50 mm in thickness for welding studies. Standard heat treatments, consisting of solution treatment at 415 °C for 2 to 10 hours (depending on the plate thickness) followed by a water quench, were performed on these plates to ensure a similar starting condition. Fully recrystallized and equiaxed grains are formed, all measuring in the range of 80 $\pm$ 30 μm (a typical grain size for most commercial Mg alloys)

The three Mg-based materials were autogeneously bead-on-plate welded with the Torvac CVE63B electron-beam welding system in vacuum at 5 to 8 $\times$ 10^{-5} torr. The focused electron-beam size was determined to be around 0.2 to 0.5 mm.[19] The electron beam was consistently focused on the specimen's top surface. The electron-beam power employed was varied from 1500 to 2500 W with weld speeds of 16, 20, and 35 mm/s. Systematic electron-beam welding characterizations in terms of microstructure and texture studies were conducted on the plates of 30 mm in thickness, using a fixed, medium electron-beam power of 1925 W, with an applied voltage of 55 kV and current of 35 mA. Selected trials were made on the 50-mm-thick plates in order to achieve thicker weld depths. The related welding parameters for this case are listed in Table II. Conventional gas tungsten arc welding was performed using Ar atmosphere protection, under a no-preheat and no-filler autogeneous bead-on-plate welding condition. The heat input for gas tungsten arc welding (98 J/mm) was chosen to be compatible with that for electron-beam welding (55 to 120 J/mm). The welding variables are also listed in Table II. Due to the Ar gas continuously flowing, minor heat dissipation *via* the Ar atmosphere is involved.

Basic characterizations such as microstructure, FZ aspect ratio, possible porosity, and crack formation were investigated by optical microscopy and scanning electron microscopy. The specimen sampling from the welded plates in terms of the three orientations (namely, the welding direction (WD), normal direction (ND), and transverse direction (TD)) for tensile testing and local texture experiments are depicted in Figure 1. The gage section of the tensile specimen is 5.5 in length, 3 mm in width, and 2 mm in thickness. For the gas tungsten arc welded (GTAW) specimens containing shallow FZs, the tensile specimens were ground away from the unpenetrated bottom part, so the thickness would be lower than 2 mm. For grain-size examinations, the welded plates were sectioned and mounted in Bakelite. The specimens were then polished using standard metallographic procedures with up to 0.05 μm Al$_2$O$_3$ powders, followed by ultrasonic vibration cleaning. The specimens were

Table I. Chemical Compositions in Weight Percent of the Three Mg-Based Materials Studied (the Atomic Percent is Shown in Parentheses)

Material	Mg	Al	Zn	Mn	Si	Fe
AZ31	bal	2.86 (2.60)	0.82 (0.31)	0.31 (0.14)	<0.01	<0.01
AZ61	bal	5.88 (5.36)	0.74 (0.28)	0.28 (0.13)	<0.01	<0.01
AZ91	bal	9.07 (8.29)	0.62 (0.23)	0.33 (0.15)	<0.017	<0.003

Table II. Welding Parameters Used for the AZ31, AZ61, and AZ91 Mg Plates for Systematic Characterization on the FZ Microstructure and Texture

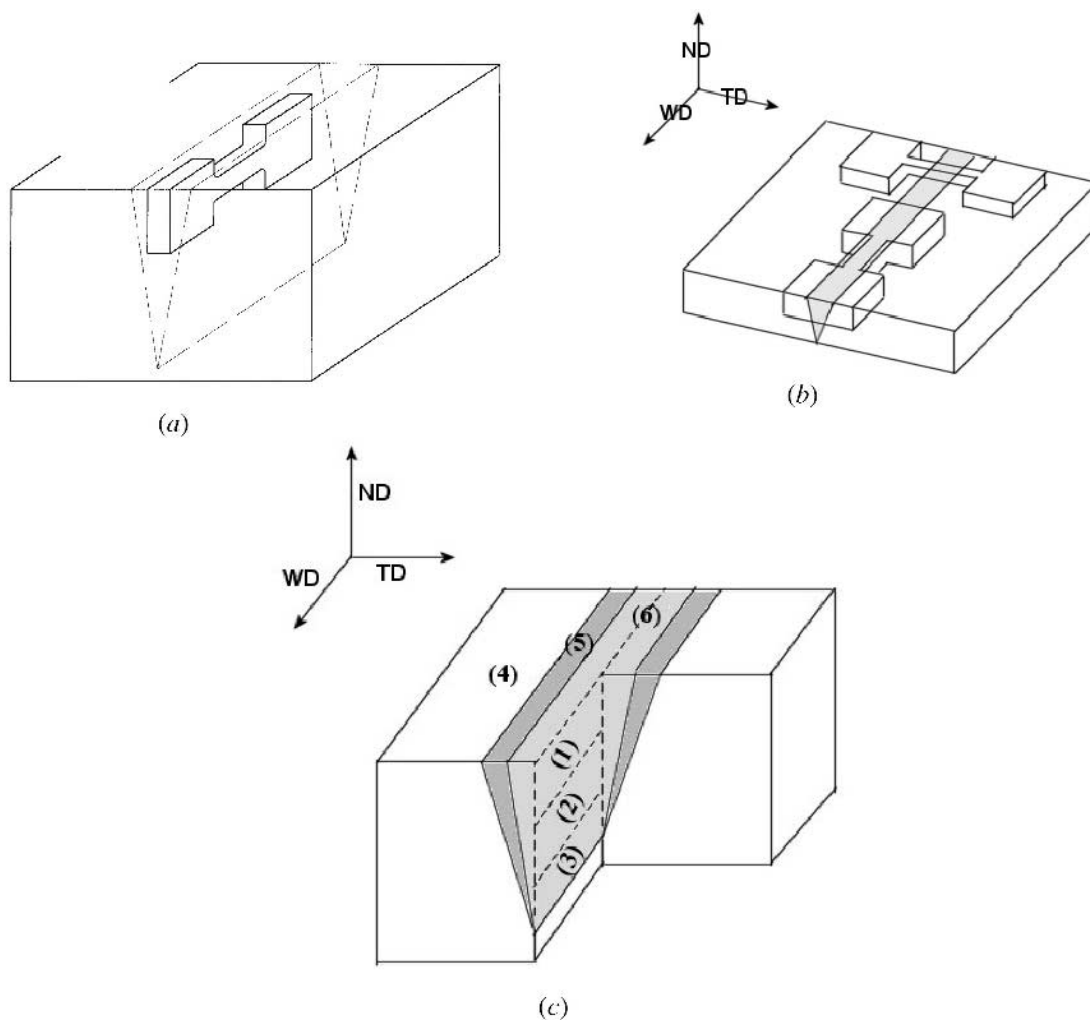| Welding method	Thickness (mm)	Voltage (V)	Current (A)	Power (W)	Speed (mm/s)	Heat Input (J/mm)
EBW	50	55,000	0.044	2400	16	150
	30	55,000	0.035	1925	16	120
					20	96
					35	55
GTAW	3	12	50	600	6.15	98

Fig. 1—Schematic drawings of the specimens extracted from the FZ: (*a*) the longitudinal minitensile EBW specimens with the loading direction parallel to WD, (*b*) the longitudinal and transverse minitensile GTAW specimens, and (*c*) small square samples for EBSD examinations. For the deep EBW FZ, the top (1), mid (2), and bottom (3) regions were examined separately. For the shallow GTAW FZ, only the fusion line (5) and FZ center (6) were included. The texture in the matrix (4) was characterized before welding.

then etched in a solution comprised of 5 mL acetic acid + 5 g picric acid + 10 mL water and 100 mL ethyl alcohol for 10 to 30 seconds until the microstructure was revealed. The linear-intercept method was used for the determination of grain size. The microhardness was measured on welded specimens after polishing to identify the softening or hardening effect within the FZ and the HAZ, using the Vickers microhardness tester with a 100 g load for a 15-second dwell time. Room-temperature tensile tests were conducted using an Instron 5582 universal testing machine at a strain rate of 1×10^{-3} s^{-1}.

Furthermore, the texture in different locations of the three Mg-based specimens before and after electron-beam welding and gas tungsten arc welding was characterized by X-ray diffraction (XRD) and electron-backscattered diffraction (EBSD) using a scanning electron microscope (SEM). The local EBSD experiments were performed using the two Oxford Opal and Inca systems, one attached to the regular SEM (JEOL* JSM 6400) and one to the field-emission-gun

---

*JEOL is a trademark of Japan Electron Optics Ltd., Tokyo.

SEM (JEOL JSM 6335). The specimens need to be carefully electrochemically polished and examined soon after polishing. Due to the low efficiency of backscattered electrons and, thus, the low intensity of the Kikuchi patterns from the low-atomic-number-element Mg, a longer accumulation time is needed. Before automatic Kikuchi-patterns indexing during the mapping and pole-figure generation is performed, frequent manual indexing to ensure the accuracy of orientation identification is strongly recommended. The pixel size was typically around 1 μm, and around 4000 pixel points were measured for each mapping and for the construction of each pole figure, inverse pole figure, and orientation distribution function (ODF). On average, around 800 grains were included for each pole-figure construction, and several locations for each region (*e.g.*, top, mid, and bottom regions of the FZ) were selected to ensure the representative accuracy and reproducibility of the constructed pole figures, and the results are confirmed by the bulk XRD pole figures. The accumulation time for one pole figure would be roughly 4 and 0.5 hours for the regular and field-emission gun SEMs, respectively.
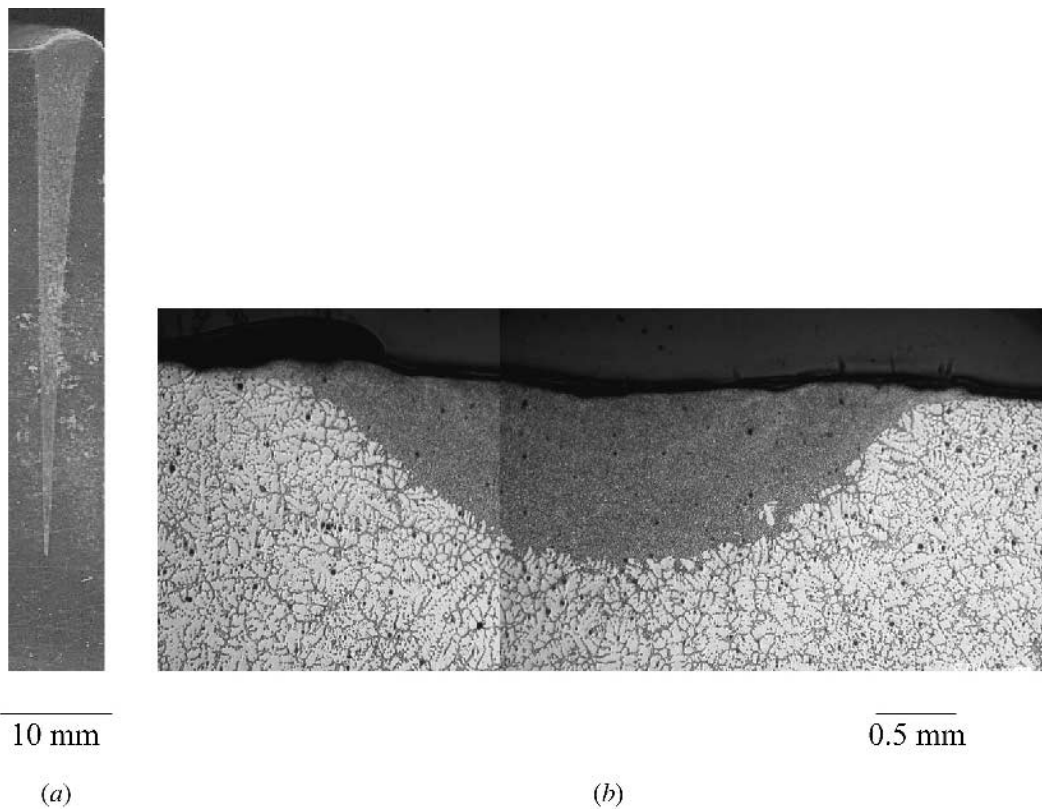
Fig. 2—Optical micrographs showing (a) the narrow and deep FZ in the EBW AZ61 specimens and (b) the wide and shallow FZ in the GTAW AZ61 specimens.

III. RESULTS

A. *Weld Appearance*

Since the Zn contents in AZ31, AZ61, and AZ91 are basically similar, the primary composition difference is the Al content. With increasing Al content from 3 to 9 pct in the three Mg-based materials, the top-surface appearance became smoother, with regular ripples and less spattering the FZ aspect ratio became higher, and the weld depth became deeper. The weld depth varied from 13 mm (43 pct penetration) to 28 mm (93 pct) for the 30 mm electron-beam-welded (EBW) specimens using heat inputs of 55 to 120 J/mm and from 1.2 mm (41 pct) to 1.4 mm (46 pct) for the 3 mm GTAW specimens using a heat input of 98 J/mm. The highest weld depths of 41, 45, and 50 mm (Figure 2(a)) were obtained in the AZ31, AZ61 and AZ91 50-mm-thick plates, respectively, using a heat input of 150 J/mm. The highest weld aspect ratio reached ~10, which is considerably high compared with Fe- and Al-based alloys. The lower solidus temperatures and the lower thermal conductivity should be the primary cause for a deeper weld depth in AZ91 with a higher Al content, as discussed previously.[18] The excellent FZ aspect ratio in EBW Mg alloys provides promising warranty for welding thick Mg plates, bars, or tubes. Figure 3 shows the variation of FZ aspect ratio in the EBW specimens as a function of heat-input level. With increasing heat input, a higher aspect ratio was obtained. Weld-induced porosity was seldom observed. Occasionally, there were one or two small pores retained at the FZ roots. This may be caused by the trapping of Mg evaporation inside the keyhole when the welding speed or cooling rate was high.
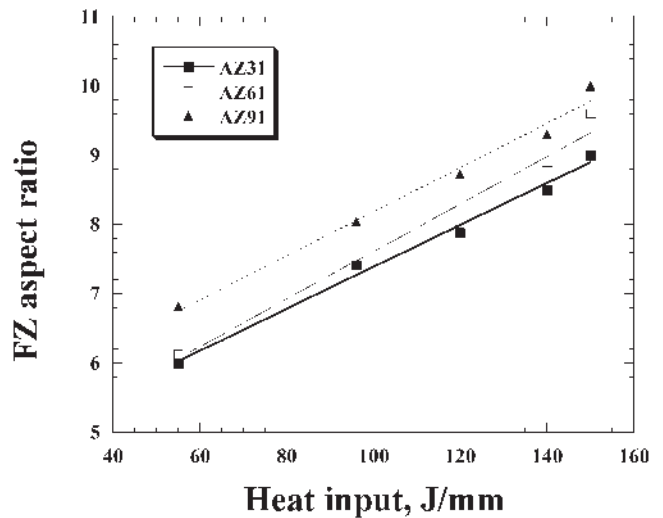

Fig. 3—Variation of FZ aspect ratio as a function of heat input for the three Mg EBW specimens.

In comparison, with a similar level of heat input of 98 J/mm (a weld power of 600 W and a weld speed of 6.15 mm/s) used in gas tungsten arc welding on the same Mg alloys, the FZ depth (~1.3 mm) and aspect ratio (~0.5) are significantly lower, as shown in Figure 2(b). The keyhole mechanism did not operate during gas tungsten arc welding. Apparent spattering was observed on the AZ31 GTAW weld surface. With increasing Al content, the top surface became smoother with stable ripples, a similar behavior to the EBW specimens.
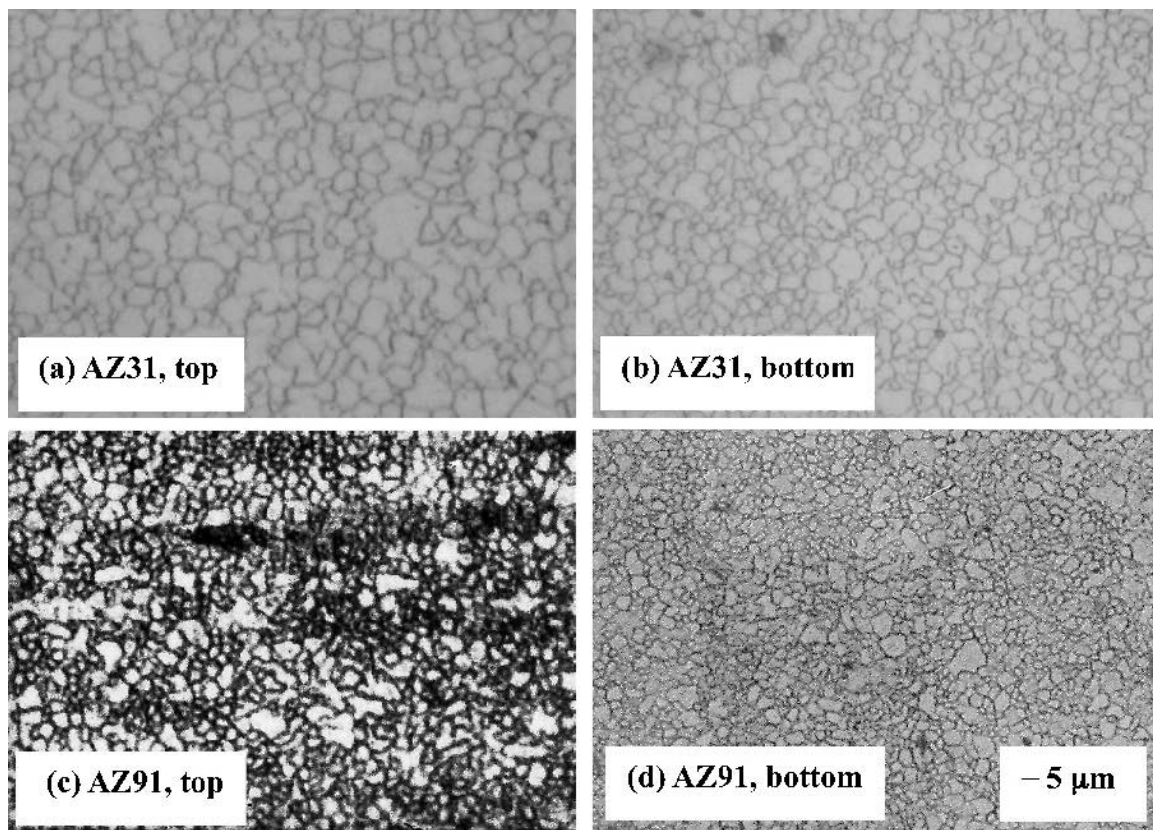
Fig. 4—Optical micrographs showing the grain structures in the (*a*) and (*c*) top and (*b*) and (*d*) bottom regions of the AZ31 and AZ91 EB FZs welded with a heat input of 96 J/mm.

Table III. Summary of the Measured Grain Size (μm) in the Top, Mid, and Bottom Regions of FZ in the Three Mg Alloys Subject to EBW and GTAW; the Data Are Subjected to a Maximum 10 Pct Standard Deviation

| Material	Welding Method	Heat Input (J/mm)	Top	Mid	Bottom
AZ31	EBW	55	9.2	8.0	6.1
		96	10.0	8.1	6.9
		120	15.3	13.0	8.9
	GTAW	98	—	12.1	—
AZ61	EBW	55	7.3	6.2	5.4
		96	8.8	7.6	6.0
		120	11.1	8.0	6.9
	GTAW	98	—	9.7	—
AZ91	EBW	55	5.0	4.1	2.9
		96	5.3	5.0	4.2
		120	7.2	6.1	4.4
	GTAW	98	—	8.0	—

B. *FZ Microstructures*

Figure 4 presents the typical optical micrographs showing the FZ grain structures. Table III compares the grain sizes measured from the top, mid, and bottom regions of the deep FZ in the EBW 30 mm specimens subject to different heat-input levels. The grain size shows a decreasing trend with decreasing heat input, increasing Al content, and increasing distance from the top surface. The aforementioned trend can be easily understood in terms of the lower degree of grain growth with lower heat input and the faster cooling rate in the root area. For all three alloys EBW using a weld power of 1925 W in the 30-mm-thick plate, the grain size in the bottom regions falls to 3 to 9 μm, appreciably reduced from the 80 $\pm$ 30 μm size in the matrix. There was no apparent long columnar grain in all EBW specimens. The lack of long columnar grains is thought to be a result of high thermal conductivity and high cooling rates in Mg alloys, as discussed previously.[18]

In comparison, with a similar level of heat input of 98 J/mm applied in gas tungsten arc welding on the same Mg alloys, the grain size was larger than that in the EBW counterparts, as compared in Table III. Due to the shallow FZ in the GTAW specimens, the grain sizes for the GTAW specimens in Table III represent the typical readings obtained from the entire FZ. There was no apparent variation in the top or bottom FZ region.

The fusion line between the FZ and matrix in both of the EBW and GTAW specimens becomes more and more vague and extends into the matrix with increasing Al content, as compared in Figure 5. This was especially pronounced in AZ91, with the highest solute contents; in this case, the fusion line appears to be a wide, partially liquated zone near the fusion boundary. According to the Mg-Al phase diagram[20] in Figure 6, the liquid + solid dual-phase temperature range increases with increasing Al content. In the AZ91 alloys, partial melting would proceed from the FZ outward along the β precipitates that were mainly aligned along the grain boundaries of the base materials. The low-melting-point nature ($T_m \sim$ 450 °C) of the β precipitates, coupled with the high thermal conductivity and low heat capacity of Mg-based alloys, lead to the wide partial melting zone. In contrast, with the low Al content and
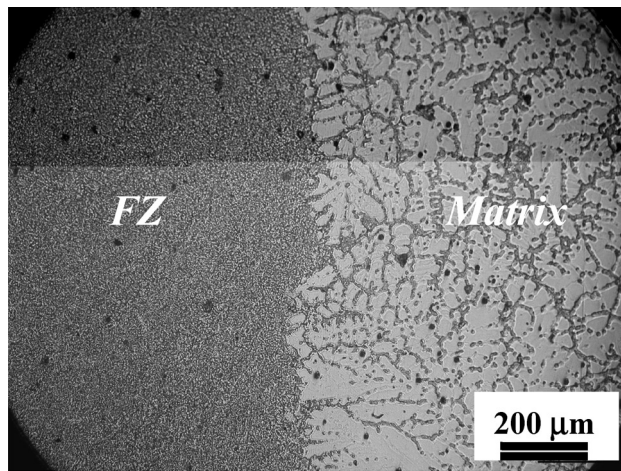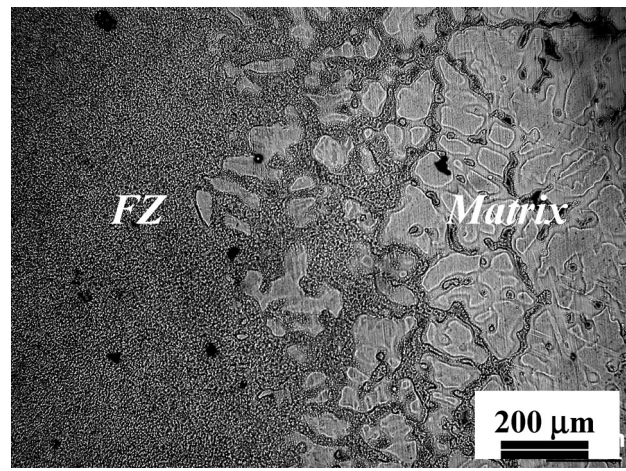
Fig. 5—Optical micrographs showing (*a*) the distinct and straight fusion line in AZ31, and (*b*) extended partial melting and zigzag fusion line in AZ91 subject to EBW or GTAW.
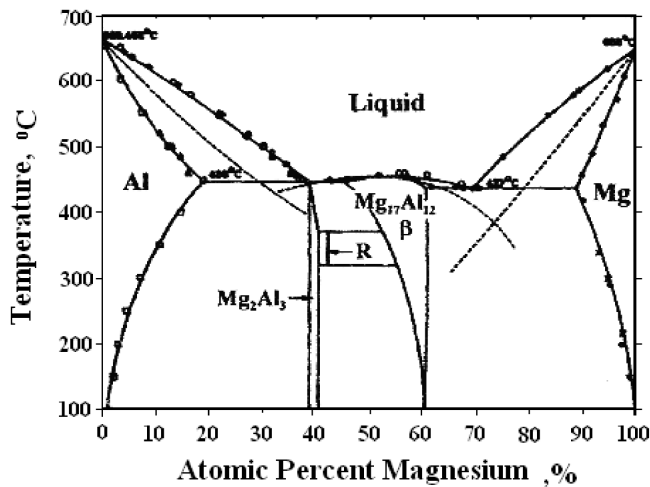

Fig. 6—Binary phase diagram of the Mg-Al system.[20]

Table IV. Summary of the Measured Microhardness (H_v) in the Top, Mid, and Bottom Regions of FZ in the Three Mg Alloys Subject to EBW and GTAW; the Average H_v Microhardness Data on the Unwelded Base Metals are 56, 60, and 68 for AZ31, AZ61, and AZ91, Respectively

Material	Welding Method	Heat Input (J/mm)	Top	Mid	Bottom	Weld Efficiency
AZ31	EBW	55	64	69	71	123 pct
		96	62	67	67	120 pct
		120	57	63	64	113 pct
	GTAW	98	—	55	—	98 pct
AZ61	EBW	55	74	73	75	122 pct
		96	70	73	78	122 pct
		120	70	72	72	120 pct
	GTAW	98	—	65	—	108 pct
AZ91	EBW	55	81	82	85	121 pct
		96	80	82	84	121 pct
		120	78	80	80	118 pct
	GTAW	98	—	75	—	110 pct

Table V. Summary of the Measured Tensile Properties of the Fusion Zone of the Three Mg Alloys Subject to EBW and GTAW; the Average UTS and Elongation Values of the Unwelded Base Metals are 201 MPa and 18 Pct, 211 MPa and 15 Pct, and 216 MPa and 13 Pct for AZ31, AZ61, and AZ91, Respectively

Material	Welding Method	Heat Input (J/mm)	UTS (MPa)	Elongation (Pct)	Weld Efficiency
AZ31	EBW	55	240	21	119 pct
		96	238	26	118 pct
		120	217	24	108 pct
	GTAW	98	210	25	104 pct
AZ61	EBW	55	264	19	125 pct
		96	261	16	124 pct
		120	258	10	121 pct
	GTAW	98	205	11	97 pct
AZ91	EBW	55	270	11	125 pct
		96	265	10	123 pct
		120	258	10	119 pct
	GTAW	98	213	10	99 pct

possessing minimum β precipitates in both the FZ and base matrix of the AZ31 alloy, there was no apparent partial melting along the precipitate stringers or grain boundaries.

C. *Postweld Mechanical Properties*

Microhardness measurements were carried out on the postweld specimens along both the horizontal and vertical directions of the FZ. The average data on both the EBW and GTAW specimens are compared in Table IV. The hardness reading shows an increasing trend with decreasing heat input, increasing Al content, and increasing distance from the top surface. The hardness exhibits a reversed trend against that observed from the grain size, which can be rationalized on the basis of the Hall–Petch relationship, as discussed in Section IV–A. The microhardness readings of the GTAW specimens are slightly lower than those of the EBW counterparts, consistent with their slightly larger grain size. From Table IV, it is apparent that the weld efficieny (defined by the postweld microhardness at the mid-FZ region divided by that of the unwelded base metal) for the EBW and GTAW

specimens varies from 113 to 123 pct and 98 to 110 pct, respectively. The high weld efficiency is partly due to the fact that the unwelded base metals were all billet products directly machined from the semicontinuous casting product. The latter is intrinsically softer. Our previous studies[18] on the extruded or rolled Mg plates yielded a relatively lower weld efficiency of 80 to 110 pct.

Tensile tests were performed using mini tensile specimens extracted from the EBW and GTAW specimens (Figures 1(a) and (b), with tensile loading direction being parallel or perpendicular to the welding direction; these are called the longitudinal or transverse mini tensile specimens. For the longitudinal specimens, it was found that most postweld tensile-strength values were higher than those of the unwelded base metal. This was confirmed by the fact that almost all transverse specimens failed in the matrix, rather than inside the FZ, implying that the FZ is stronger than the matrix. The tensile data presented in Table V are those averaged from the longitudinal-specimen results and are considered to correspond to the true strength of the FZ. It can be seen from
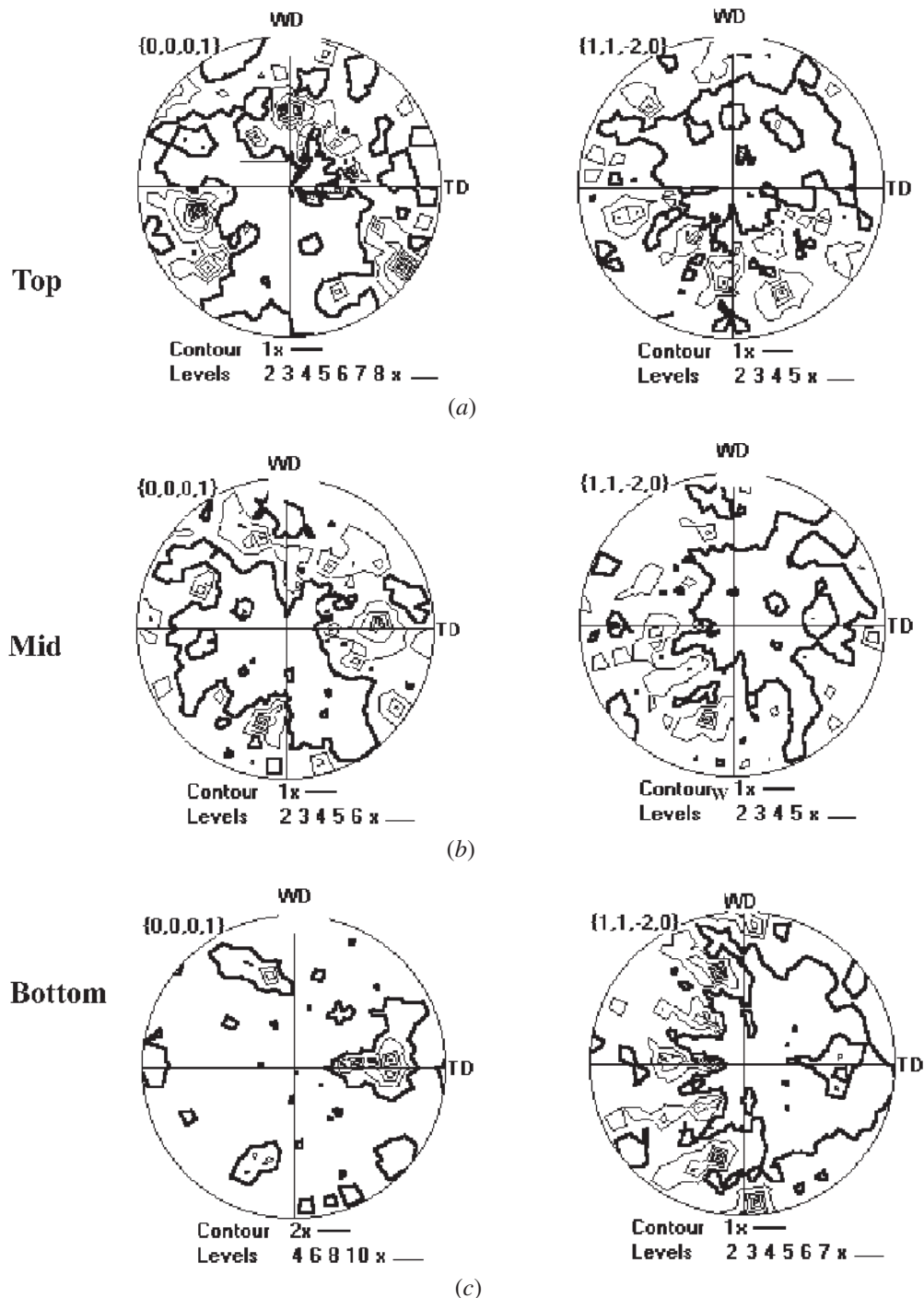

Fig. 7—Typical EBSD (0001) and $(11\bar{2}0)$ pole figures obtained from the (a) top, (b) mid, and (c) bottom regions of the AZ61 FZ EB welded at 1925 W and 16 mm/s.

Table V that the weld efficiency (defined by the postweld ultimate tensile stress (UTS) divided by the UTS of the unwelded base metal) for the EBW and GTAW specimens varies from 108 to 125 pct and 97 to 104 pct, respectively, consistent with the microhardness results. The tensile elongation of the EBW and GTAW specimens did not degrade as compared with the unwelded base metals.

D. *The EBSD Texture Characterizations*

1. *The EBW specimens*

The EBSD pole figures represent the local texture within a smaller region, usually measuring $\sim 200 \times 200$ μm^2. For the EBW specimens with a deep FZ, the grain-orientation distributions were measured from the top, mid, and bottom areas of the FZ. The texture was measured from the three locations of the longitudinal plane consisting of the WD and ND, as shown by positions 1 through 3 in Figure 1(c). For the GTAW specimens, since the FZ is rather wide and shallow, the fusion line and FZ center of the top surface or the welding plane consisting of the WD and TD were selected for EBSD measurements, as also depicted by positions 5 and 6 in Figure 1(c). The EBSD software will transform the input orientations and present the pole figures in terms of WD and TD axes, representing the top surface or welding plane of the FZ.

Numerous pole figures, *i.e.*, (0001), ($10\bar{1}0$), ($11\bar{2}0$), ($11\bar{2}1$), and ($11\bar{2}2$) (and inverse pole figures and ODF as well), would be generated from each mapping. Figure 7 presents an example of the (0001) and ($11\bar{2}0$) pole figures, obtained from the top, mid, and bottom regions of the EBW AZ61 specimen with a welding power of 1925 W and welding speed of 16 mm/s. The maximum contour level in the pole figures is, at most, 10 against the background, which is not considered to be a highly strong texture, judging from a much higher level of up to 40 reached for severely rolled or extruded alloys.[21,22] Intuitively, the presence of numerous equiaxed grains in the current FZ should not involve significantly strong textures. However, an appreciable degree of preferred orientation with the medium level of 2 to 10 is consistently observed. Upon comparing these pole figures with the ideal texture components simulated by an internal self-written software[23] (*e.g.*, Figure 8) and standard stereography projections for pure Mg (with *c/a* ratio of 1.624), three major texture components were identified for this case. Their relationship with the FZ orientations is established as

Type A: $\{10\bar{1}1\}<10\bar{1}\,\bar{2}>$ texture component,
TD//$<11\bar{2}0>$ [1a]

Type B: $\{11\bar{2}1\}<1\bar{1}00>$ texture component,
ND $\wedge$ $<11\bar{2}0>\sim$15 deg   [1b]

Type C: $\{10\bar{1}0\}<11\bar{2}2\,>$ texture component,
WD $\wedge$ $<11\bar{2}0>\sim\sim$30 deg   [1c]

The symbol $\wedge$ refers to the angle relationship between the two mentioned orientations. Note that, in the type-A texture, with $\{10\bar{1}1\}$ parallel to the welding plane and $<10\bar{1}\,\bar{2}>$ parallel to the WD, then the TD has to be parallel to the *a*-axis (*i.e.*, $<11\bar{2}0>$). Mean while, the ND in the type-B texture is $<11\bar{2}1>$, which is $\sim$15 deg with respect to the *a*-axis $<11\bar{2}0>$, and the WD in the type-C texture is $<11\bar{2}2>$, which is $\sim$30 deg with respect to the *a*-axis $<11\bar{2}0>$. Figure 9

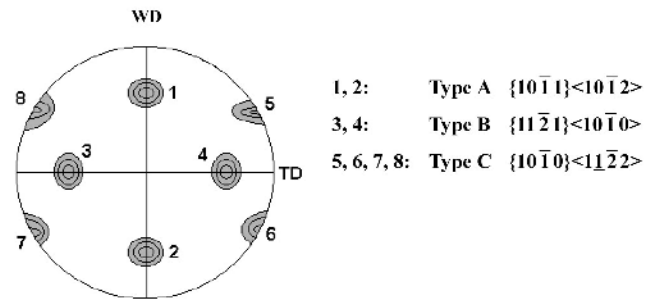
Fig. 8—The ideal positions of the three main texture components, types A, B and C, in the {0001} pole figure of Mg simulated by an internal software.[21]
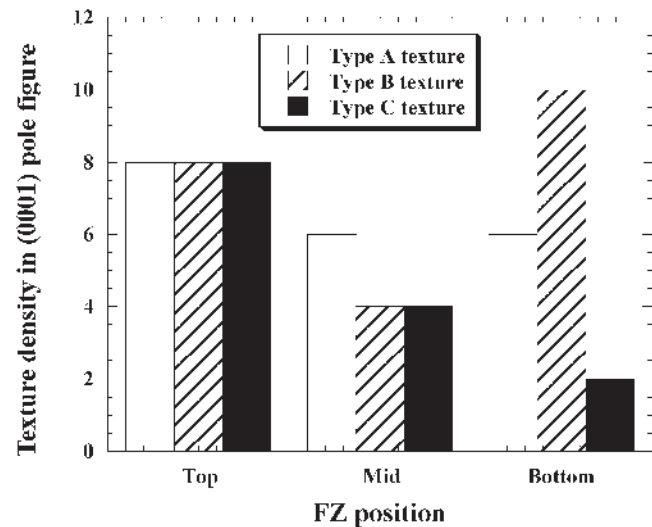

Fig. 9—The variation of texture intensity for the three main texture components as a function of FZ position in the AZ61 specimens EB welded at 1925 W and 16 mm/s.

shows the intensity variations of the three texture components as a function of FZ position for this very specimen. The contour intensity levels vary from 2 to 10. For a nearly random grain-orientation distribution, the intensities usually show minor variations from 1 to 3.[22] Due to mainly the cooling rate and heat-flow conduction direction, as discussed in Sections IV–B and C, there are texture variations in different positions. The exact intensities for the three major texture components do show minor variations, but usually the intensities are higher for the FZ top region (suggesting more mature development of the preferred orientation).

Systematic EBSD examinations on the three alloys subject to three different electron-beam welding speeds have reached the conclusion that the cooling rate would impose the greatest influence on the texture. The texture difference due to FZ location (top to bottom region), welding speed (16 to 35 mm/s), and alloy composition (AZ31 to AZ91) can all be combined and rationalized by mainly the cooling-rate factor. As discussed in Section IV–B, the cooling-rate sequences are

$$\text{Bottom} > \text{mid} > \text{top} \qquad [2a]$$

$$35 \text{ mm/s} > 20 \text{ mm/s} > 16 \text{ mm/s} \qquad [2b]$$

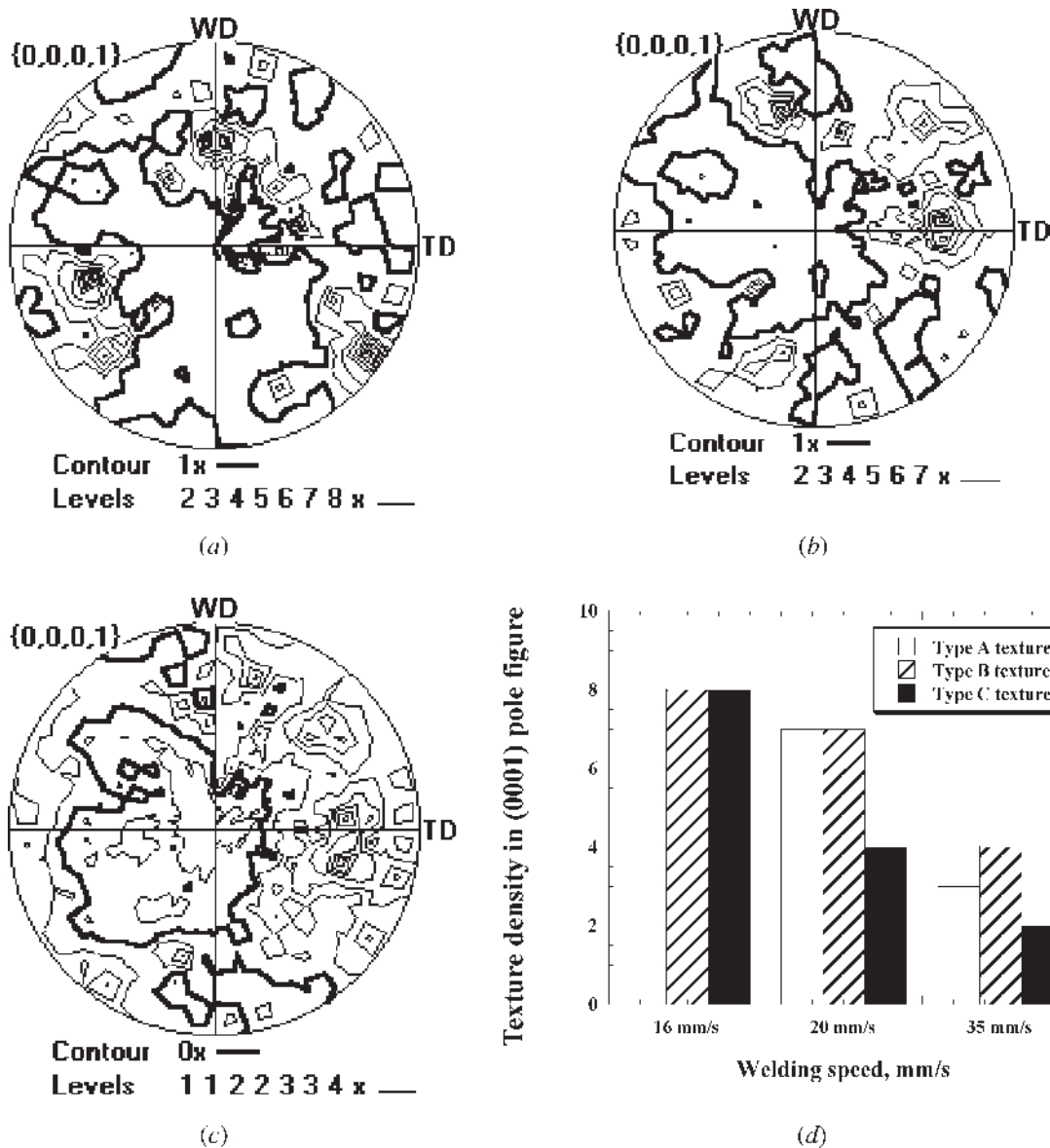$$\text{AZ31} > \text{AZ61} > \text{AZ91} \qquad [2c]$$

Fig. 10—EBSD (0001) pole figures constructed from the top FZ region in the AZ61 specimens EB welded at 1925 W and (*a*) 16 mm/s, (*b*) 20 mm/s, and (*c*) 35 mm/s. (*d*) The variation of texture intensity as a function of welding speed.

Figure 9 has shown the effect from the FZ position, using AZ61 as example. The effect from welding speed is compared in Figure 10. With increasing weld speed (*i.e.*, with a higher cooling rate), all texture components became less developed (weaker in intensity). Finally, the effect from alloy content (mainly from Al content) on the texture was found to be less pronounced, as shown in Figure 11.

2. The GTAW specimens

The texture in GTAW specimens was appreciably less intense than that observed in the EBW specimens. Since the FZ in GTAW specimens is wide and shallow, EBSD was done only for the FZ center and fusion line on the top surface after grinding. Typical pole figures are shown in Figures 12(a) and (b). There are a number of weak texture components identified, such as $\{11\bar{2}1\}<0\bar{1}1\bar{1}>$, $\{0\bar{1}10\}<\bar{2}113>$, $\{01\bar{1}\,\bar{2}\}<0\bar{1}1\bar{1}>$, and $\{10\bar{1}\,\bar{1}\}<10\bar{1}2>$. The relative intensities for the main components in these three alloys are compared in Figure 12(c). In the

AZ61 and AZ91 alloys, due to the even lower cooling rate (Section IV–B), other very minor texture components were traced, such as $\{10\bar{1}0\}<0001>$ and $\{10\bar{1}0\}<11\bar{2}0>$, making the pole figures and ODFs rather complicated. Meanwhile, the texture in the FZ center also appears to be more complicated than that in the fusion line, since the cooling rate in the former is also lower than that in the latter.

IV. DISCUSSION

A. On the Postweld Mechanical Properties

Overall, the weld efficiency in terms of both hardness and UTS for the EBW and GTAW specimens is satisfactory. Due to the effective grain refinement and minimum porosity or hot cracking inside the FZ, welding not only did not degrade the material properties, but it also strengthened the weld piece with no loss of ductility. The average microhardness
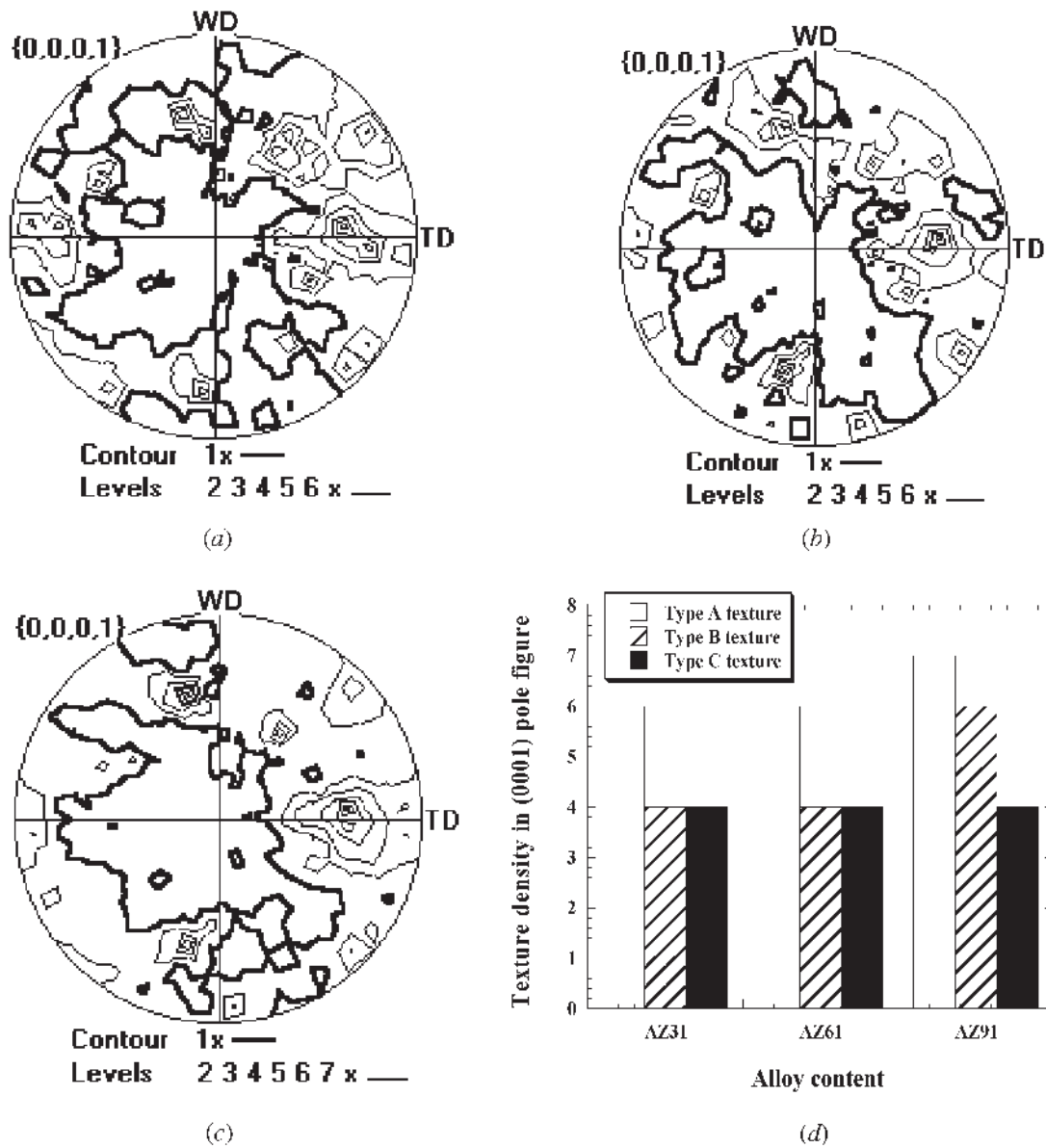
Fig. 11—EBSD (0001) pole figures constructed from the mid FZ region in the three Mg alloys EB welded at 1925 W and 35 mm/s: (*a*) AZ31, (*b*) AZ61, and (*c*) AZ91. (*d*) The variation of texture intensity as a function of alloy content.

data (in units of H_v) inside the FZ are plotted against the grain-size term $d^{-1/2}$ (in $\mu m^{-1/2}$) in Figure 13(a). Although scattering exists, the Hall–Petch relationship is followed. On average, the microhardness can be expressed as

$$H_{v,AZ31} = 33 + 95\, d^{-1/2} \qquad [3a]$$

$$H_{v,AZ61} = 50 + 59\, d^{-1/2} \qquad [3b]$$

$$H_{v,AZ91} = 63 + 38\, d^{-1/2} \qquad [3c]$$

It can be said that the current high weld efficiency is primarily a result of grain-size refinement in the rapidly solidified FZ. Due to other factors related to microdefects and elongations, which would more sensitively affect the UTS than the hardness, it is difficult to define the increasing trend

But, the yield-stress (YS) data (in units of megaPascals) fit well with the Hall–Petch relationship, as plotted in Figure 13(b). The data can be expressed as

$$YS = 117 + 260\, d^{-1/2} \qquad [4a]$$

$$YS = 130 + 231\, d^{-1/2} \qquad [4b]$$

$$YS = 137 + 205\, d^{-1/2} \qquad [4c]$$

The K slope in the previous equation (205 to 260 MPa· $\mu m^{1/2}$) is in fair agreement with previously reported values of 210 MPa·$\mu m^{1/2}$[24] and 307 MPa·$\mu m^{1/2}$[25,26] for the Mg alloys. Note that the YS and UTS data would also be affected by the β phase and the dissolved solute amounts, in addition to the grain size; the former factors are not rigorously considered in this study.
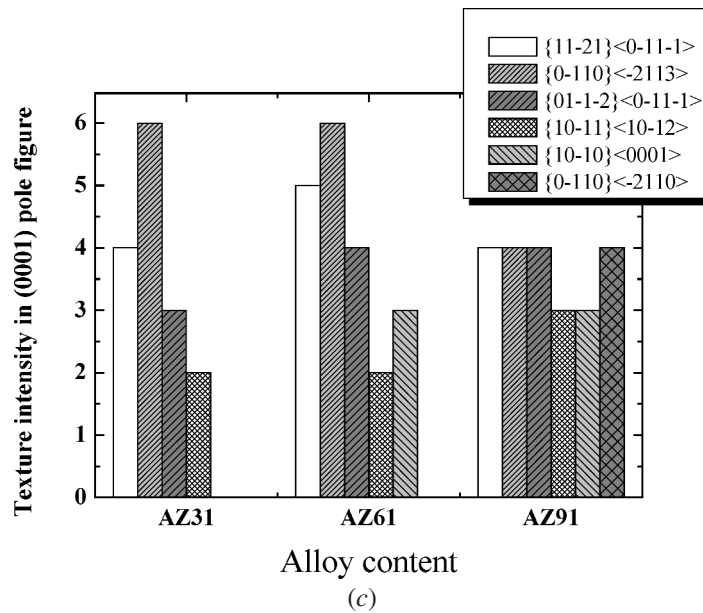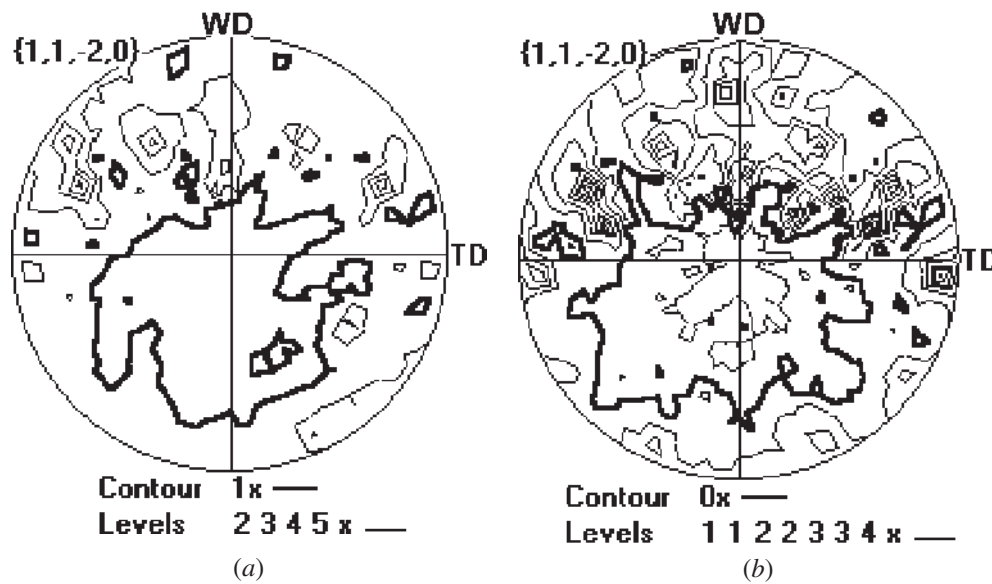
Fig. 12—Examples of the EBSD $(11\bar{2}0)$ pole figures constructed from (*a*) the FZ center and (*b*) the fusion line boundary region in the AZ31 specimens GTAW at 600 W and 6.15 mm/s. (*c*) The variation of texture intensity as a function of alloy content.

B. *Cooling-rate Evaluation*

The cooling rate appears to strongly affect the weld microstructure and texture. In estimating the cooling rate during EBW and GTAW for the three alloys under different weld speeds, it is necessary to consider the major heat-flow directions. Since the thickness of the EBW specimen (30 mm) is considerably higher than that of the GTAW specimen (3 mm), and the FZ penetration degree also varies from 43 pct (13 mm) to 93 pct (28 mm) for the EBW specimen and from 41 pct (1.2 mm) to 46 pct (1.4 mm) for the GTAW specimen, the actual heat flow might vary from the pure two-dimensional (2-D) to pure three-dimensional (3-D) models, depending on the relative thickness in various specimens. Using the simplified 2-D and 3-D models,[27,28,29] the

lower and upper bounds of the cooling rate (R) can be estimated by the following equations:

$$\text{3-D (lower bound): } R = \frac{dT}{dX}\,V = \frac{2\pi K}{H}(T - T_0)^2 \quad [5a]$$

$$\text{2-D (upper bound): } R = \frac{dT}{dX}\,V = 2\pi K\rho C_p\left(\frac{h}{H}\right)^2(T - T_0)^3 \quad [5b]$$

where X is the spatial distance, V is the weld speed, ρ is the materials' density, K is the thermal-conductivity coefficient for the solid, h is the specimen thickness, and H is the heat input. Using the thermal parameters for the three Mg-based alloys in Table VI, the lower and upper bounds
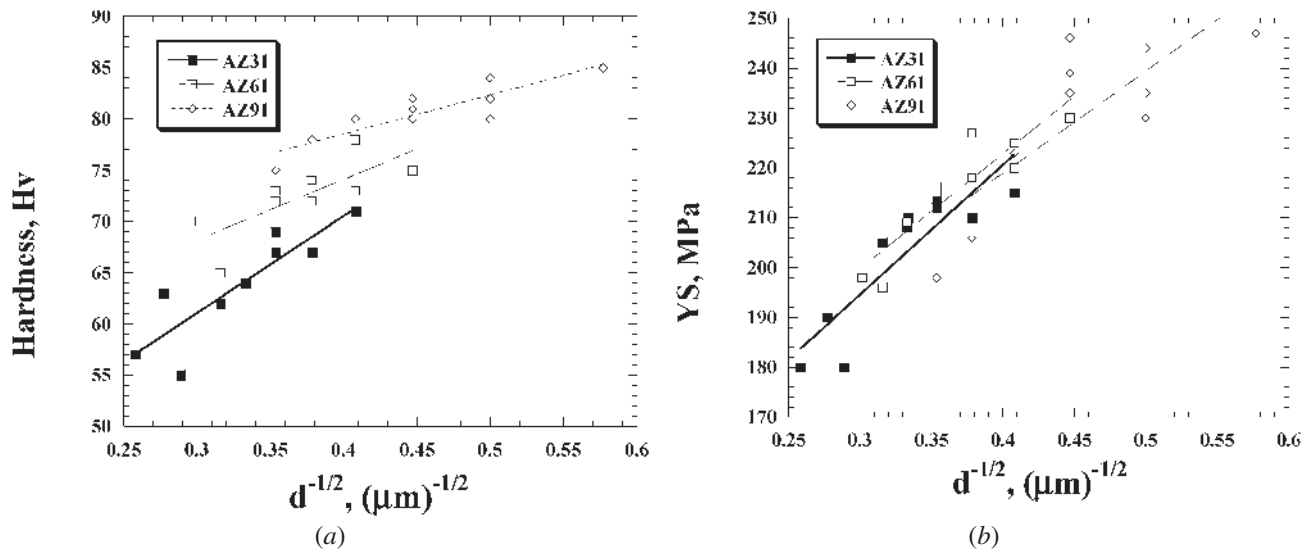
Fig. 13—Variations of (*a*) microhardness and (*b*) yield stress of the three Mg alloys subject to EBW or GTAW as a function of the inverse square root of grain size.

Table VI. The Thermal Related Properties of the Pure Mg and Three Mg-Based Alloys

Material	Density (g/cm^3)	Thermal Conductivity (W/m K)	Heat Capacity (J/g K)	Thermal Diffusion (m^2/s)	Special heat of Fusion (J/g)	Melting Range (°C)
Pure Mg	1.74	152.8	1.00	8.87×10^{-5}	368.4	650
AZ31	1.78	76.9	0.99	4.36×10^{-5}	339.1	575 to 630
AZ61	1.80	64.1	0.99	3.63×10^{-5}	354.5	530 to 610
AZ91	1.81	51.4	0.98	2.89×10^{-5}	370.0	470 to 595

of the cooling rate were determined for two temperatures, one at 650 °C, near the melting temperature, and another at 1000 °C, a temperature below the boiling point of 1107 °C for pure Mg. The calculated results for the EBW and GTAW specimens are listed in Table VII. The cooling 2-D model for the major heat flows along the WD and TD might apply better in the EBW specimens with deep FZs, whereas the 3-D model is more feasible in the GTAW specimens. Cooling rates during gas tungsten are welding are typically of the order of 10^1 to 10^2 °C/s, lower than those during electron-beam welding by 50 to 100 times. Nevertheless, due to the continuous blowing of the Ar gas onto the back surface of the Mg sheet for protection during gas tungsten are welding, a certain degree of heat release by Ar gas is expected, especially for the back surface.

Combining the effects from alloy content and welding speed, the overall sequence for the cooling rate during electron-beam welding is AZ31-35 > AZ61-35 > AZ91-35 > AZ31-20 > AZ61-20 > AZ31-16 > AZ61-16 ≅ AZ91-20 > AZ91-16 . It can be seen from Table VII that the cooling rate at the high welding speed of 35 mm/s is around 2 times of that at the lower welding speed of 16 mm/s. In comparison, the higher cooling in AZ31 is around 1.5 times of that in AZ91, *i.e.*, the welding-speed influence would override the Al-content role. Furthermore, the cooling rate would increase with increasing distance from the top surface, where the heat was input. Thus, the cooling-rate sequence with respect to the FZ location would be bottom > mid > top region. The higher cooling rate at the bottom region, or at the high welding speed, would, in turn, result in a finer grain size.

C. Texture Evolution in Top, Mid, and Bottom Positions

The texture analysis of hexagonal crystals is a challenging task due to their lower symmetry than the cubic crystals. Studies on welding textures are very limited, especially on hexagonal crystals. From the microstructure observations, it is seen that the grain structures in the EBW and GTAW fusion zones are basically equiaxed owing to the rapid cooling rate, and the texture intensity is not as strong as that observed in the wrought materials after mechanical processing. Generally, it is accepted that the crystallographic growth direction of close-packed orientations would most possibly follow the heat-flow direction (or the direction along with the maximum temperature gradient).[29] During the conventional casting of metals, solidification usually commences by heterogeneous nucleation at the interface between the mold wall and liquid metal and results in the formation of grains with a wide range of crystallographic orientations; that is, a random texture develops in this interface regime.[28] Expect for the solidification under controlled heat-transfer conditions, subsequent solidification occurs by dendritic growth along preferred crystallographic directions to produce the characteristic columnar zone in casting.[30]

For the Mg-based alloys, the $<11\bar{2}0>$ *a*-axis is the most close-packed direction. It is expected that the $<11\bar{2}0>$ texture may be related to the heat-flow direction. During the welding solidification process, the heat-flow directions are very complex, possibly along the TD, ND, WD, or a combination thereof. Roughly speaking, the heat transfer should basically proceed along a direction perpendicular to the fusion boundary. Due to the high FZ aspect ratio (6 to 10) in the EBW specimens,

Table VII. Calculated Cooling Rate (R) at the Fusion Line for the Three Mg Alloys at 650 °C and 1000 °C; the 3-D and 2-D Models Were Considered to be the Lower and Upper Bounds of the Actual Cooling Rates Experienced during EBW and GTAW

Material	T, °C	Welding Method	Heat Input (J/mm)	R (°C/s) 3-D (Lower Bound)	R (°C/s) 2-D (Upper Bound)
AZ31	650	EBW	55	3.4×10^3	1.5×10^4
			96	2.0×10^3	9.5×10^3
			120	1.6×10^3	8.5×10^3
AZ61			55	2.9×10^3	1.1×10^4
			96	1.6×10^3	8.2×10^3
			120	1.3×10^3	7.5×10^3
AZ91			55	2.3×10^3	9.1×10^3
			96	1.3×10^3	7.0×10^3
			120	1.1×10^3	6.5×10^3
AZ31	650	GTAW	98	4.0×10^1	2.0×10^2
AZ61			98	3.1×10^1	1.7×10^2
AZ91			98	2.3×10^1	1.3×10^2
AZ31	1000	EBW	55	8.4×10^3	3.3×10^4
			96	4.7×10^3	2.3×10^4
			120	3.8×10^3	2.1×10^4
AZ61			55	7.0×10^3	2.7×10^4
			96	4.0×10^3	2.0×10^4
			120	3.2×10^3	1.8×10^4
AZ91			55	5.6×10^3	2.2×10^4
			96	3.2×10^3	1.5×10^4
			120	2.5×10^3	1.2×10^4
AZ31	1000	GTAW	98	1.5×10^2	7.5×10^2
AZ61			98	1.2×10^2	6.3×10^2
AZ91			98	1.0×10^2	5.0×10^2

heat flow at the vertical central line should proceed toward both the WD and TD directions for the entire top, mid, and bottom regions. In the FZ bottom region, heat flow along the ND (downward) should be more important (especially for those with a lower FZ penetration ratio less than 70 pct); thus, heat flows along both the ND and TD need to be considered together, as depicted in Figure 14(a). With further solidification, the heat flow in the FZ mid and top regions would mostly direct along the WD and TD, with gradually decreasing contributions from the ND heat flow, as shown in Figures 14(b) and (c).

Figure 15 illustrates the combined heat-flow vectors. If only the heat flow along the TD is dominant, then the TD should be parallel to the preferred growth or the close-packed direction $<11\bar{2}0>$. This is actually the case for a type-A texture, where TD $// <11\bar{2}0>$ (Figure 15(a)). If the heat flows along the ND and TD are both operating, the net vector (in between the ND and TD, with an angle of α depending on the relative magnitude of the ND and TD vectors) should be parallel to the preferred growth or close-packed direction $<11\bar{2}0>$ (Figure 15(b)). A type-B texture is consistent with this case, where the angle between the ND and $<11\bar{2}0>$ is ~15 deg. Finally, if the heat flows along the WD and TD are both operating, the net vector (in between the WD and TD) should be parallel to $<11\bar{2}0>$ (Figure 15(c)). This case is consistent with the type-C texture, in which the angle between the WD and $<11\bar{2}0>$ is ~30 deg.

Due to the complicated heat flows occurring during welding, as well as the minor variation of the local texture intensities in different locations (even within the same top or bottom region), it is difficult to describe the situation in a simplified form. But, taking the relative texture intensities presented in Figure 9 for the AZ61 EBW specimens as an example, there are still two trends revealed. First, the texture intensities in the FZ top region are usually higher, judging from Figure 9

and many other pole figures for different welded specimens. It is postulated to be a result of the longer solidification time and, thus, more-mature texture development in this region facing the incident electron beam. Second, in the bottom region, the heat flow along the ND down ward becomes overwhelming, leading the strongest type-B texture.

D. Texture Evolution in Different Alloys Subject to Different Welding Speeds

With regard to the effects of welding speed and solute content (3 to 9 pct Al), it is found that the texture characteristics and intensities are still governed mainly by the changes in the heat flow. For example, with increasing welding speed (as at 35 mm/s) or decreasing Al content (as in AZ31), the cooling rate will increase, resulting in the weakening of three texture components, as shown in Figures 10 and 11. This is because the texture did not have enough time to fully develop. In such cases, the direction and magnitude of heat flow would impose a less significant effect on the texture.

Furthermore, there might be other factors involved. The first is the effect of fusion line topography on the directions and magnitude of heat flow. Strezov and Herbertson[31] have shown that substrate topography strongly affects the degree and direction of heat flow in the melt during solidification. It should be noted that the smooth fusion boundaries present in AZ31 (Figure 5(a)) or the zigzag fusion boundaries in AZ61 and, especially, in AZ91 (Figure 5(b)) only reflect the different degree of subsequent melting back to the base metal. It does not necessarily mean that the solidification front is also uneven. Thus, the zigzag fusion boundaries might not affect the heat flow at the vertical central line where the current texture analyses were performed.

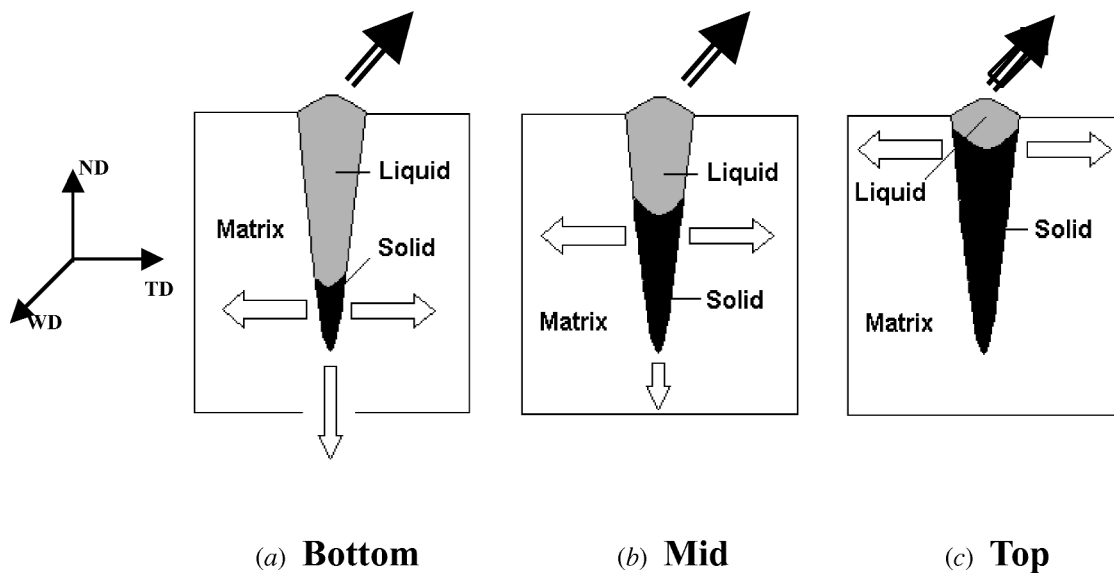(a) **Bottom**   (b) **Mid**   (c) **Top**

Fig. 14—Schematic illustration of the transfer directions of heat flow in the (a) bottom, (b) mid, and (c) top region of the FZ in the EBW specimens.
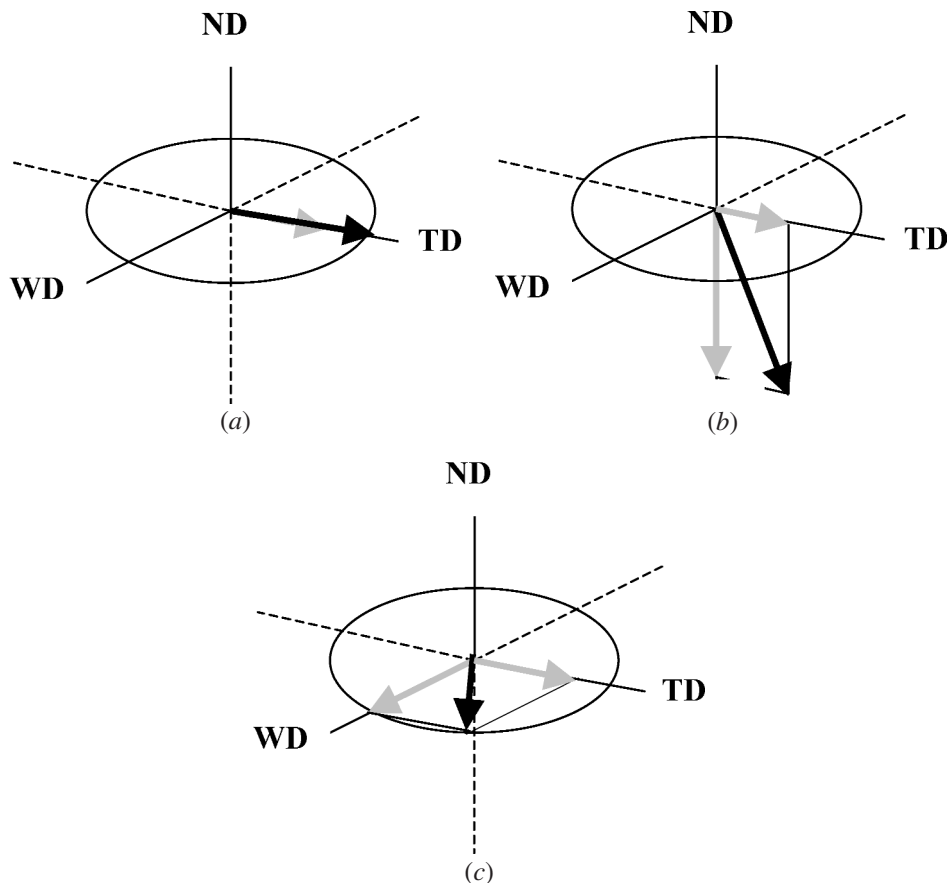

Fig. 15—Schematic drawings showing the heat flow vectors operating for the three main texture components: (a) for the type A texture, TD // <11$\bar{2}$0>; (b) for the type B texture, ND $\wedge$ <11$\bar{2}$0> ~15 deg; and (c) for the type C texture, WD $\wedge$ <11$\bar{2}$0> ~30 deg.

The second is related to the precipitation of the β phase in AZ61 and, especially, in AZ91. The Zener effect imposed by β on the grain boundaries would reduce grain growth and coalescence during the later cooling stage from 400 °C down to 250 °C, which would help in retaining the com-

plicated and diverse texture forming during rapid solidification. With more diverse textures, each texture component would also become weaker. In other words, the texture in AZ91 should be much stronger due to the lower cooling rate, but ought to be weaker due to the presence of β par-

ticles. The joint effects yield the less pronounced dependence on the resulting texture.

Finally, the texture in GTAW specimens was also more random and weaker, although the cooling rates calculated in Table VII are lower than those for electron beam welding. This is mainly due to the much smaller fusion zone, which is only ~3 mm in width and ~1.3 mm in depth. The 3-D heat flows along all three directions—the WD, TD, ND, and combinations thereof. Within such a shallow FZ region would be simultaneously operating. The texture would be highly diverse and complicated. Similar analyses using the heat-flow arguments were also made for the four major texture components, but they are much more complicated and appear less significant than the findings from the EBW specimens.

V.   SUMMARY

1. Electron-beam welding on the AZ-series Mg alloys can result in a sound FZ with an unusually narrow and deep nature, an aspect ratio up to 10, and almost no porosity and hot cracking. The high FZ depth of ~50 mm is well above those achieved in common Fe- and Al-based alloys.
2. The FZ grains are nearly equiaxed in shape and ~8 μm or less in size due to the rapid cooling rate.
3. The as-welded FZ microhardness and tensile strength are higher than the base metals due to the smaller grain size. The weld efficiency is around 110 to 125 pct for the EBW specimens and 97 to 110 pct for the GTAW specimens; both are satisfactory.
4. There are three main texture components present in the EBW FZ, i.e., $\{10\bar{1}1\}<10\bar{1}2>$ (with TD // $<11\bar{2}0>$), $\{11\bar{2}1\}$ $<1\bar{1}00>$ (with ND $\wedge$ $<11\bar{2}0>\sim$ 15 deg), and $\{10\bar{1}0\}$ $<11\bar{2}2>$ (with WD $\wedge<11\bar{2}0> \sim$ 30 deg). Attempts have been made to relate the texture to the heat-flow directions along the TD, ND, WD, or combination thereof.
5. The texture in GTAW specimens is more diverse and complicated than that in the EBW counterparts, due to the limited and shallow FZ and the lower cooling rate.
6. The cooling rates were estimated using the 3-D (lower-bound) and 2-D (upper-bound) heat-transfer models for the EBW and GTAW welds. The 2-D model might apply for the narrow and deep EBW fusion zones, and the 3-D one fits better for the broad and shallow GTAW welds. The cooling rate increases with decreasing Al content, increasing weld speed, and increasing distance from the weld top surface. The high cooling rate is considered to be the cause for the fine and equiaxed grains and the diverse textures in the fusion zone.
7. The characteristics of the oriented grain distributions inside the EBW FZ can be traced according to the direction and magnitude of the heat-flow vectors. The main weld texture characteristics are significantly influenced by the heat flow, i.e., the crystal growth tends to align toward $<11\bar{2}0>$ (the most closed-packed direction) in the hexagonal Mg-based alloys.
8. Overall, electron-beam welding is demonstrated to be a promising means of welding delicate, thick Mg plates, bars, or tubes, while gas tungsten arc welding is limited to lower-end thin Mg sheets.

REFERENCES

1. P. Villars, A. Prince, and H. Okamoto: *Handbook of Ternary Alloys Phase Diagram*, ASM INTERNATIONAL, Materials Park, OH, 1990, p. 3933.
2. S. Lee, S.H. Lee, and D.H. Kim: *Metall. Mater. Trans. A*, 1998, vol. 29A, pp. 1221-35.
3. E. Aghion and B. Bronfin: *Mater. Sci. Forum*, 2003, vols. 350–351, pp. 19-30.
4. P.G. Sanders, J.S. Keske, K.H. Leong, and G.J. Kornecki: *Laser Appl.*, 1999, vol. 11, pp. 96-103.
5. S. Juttner and H. Wohlfahrt: in *Magnesium Alloys and Their Application*, B.L. Mordike and K.U. Kainer, eds., Werkstoff mbH, Frankfurt, Germany, 1998, pp. 18-25.
6. H. Krohn and S. Singh: in *Trends in Welding of Lightweight Automotive and Railroad Vehicles*, Wels, Austria, 1997, pp. 625-26.
7. A. Stern and A. Munitz: *J. Mater. Sci. Lett.*, 1999, vol. 18, pp. 853-55.
8. J. Matsumoto, M. Kobayashi, and M. Hotta: *Welding Int.*, 1990, vol. 4, pp. 23-28.
9. V.M. Nikitin, Y.L. Skornyakov, and A.Y. Romanov: *Svar. Proiz.*, 1977, vol. 10, pp. 25-27.
10. V. Vilukin and I.S. Dobrynina: *Welding Int.*, 1998, vol. 12, pp. 801-03.
11. K. Kato and H. Tokisue: *Welding Int.*, 1994, vol. 8, pp. 452-57.
12. A. Munitz, C. Cotler, H. Shaham, and G. Kohn: *Welding J.*, 2000, vol. 32 (7), pp. 202s-208s.
13. R. Tsujino, G. Kawai, H. Ochi, H. Yamaguchi, K. Ogawa, and Y. Suga: *Mater. Sci. Forum*, 2003, vols. 426–432, pp. 3005-10.
14. H. Haferkamp, U. Dilthey, G. Trager, I. Burmester, and M. Niemeyer: in *Magnesium Alloys and Their Application*, B.L. Mordike and K.U. Kainer, eds., Werkstoff mbH, Frankfurt, Germany, 1998, pp. 595-600.
15. A. Weisheit, R. Galun, and B.L. Mordike: in *Magnesium Alloys and Their Application*, B.L. Mordike and K.U. Kainer, eds., Werkstoff mbH, Frankfurt, Germany, 1998, pp. 619-625.
16. A. Weisheit, R. Galun, and B.L. Mordike: *Welding J.*, 1998, vol. 30 (4), pp. 149s-154s.
17. U. Draugelates, B. Bouaifi, J. Bartzsch, and B. Ouaissa: in *Magnesium Alloys and Their Application*, B.L. Mordike and K.U. Kainer, eds., Werkstoff mbH, Frankfurt, Germany, 1998, pp. 601-05.
18. S.F. Su, J.C. Huang, H.K. Lin, and N.J. Ho: *Metall. Mater. Trans. A*, 2002, vol. 33A, pp. 1461-73.
19. J.R. Lin: Ph.D. Thesis, National Sun Yat-Sen University, Taiwan, 1996.
20. A.A. Nayeb-Hashemi and J.B. Clark: *Phase Diagrams of Binary Magnesium Alloys*, ASM INTERNATIONAL, Metals Park, OH, 1988, pp. 18-27.
21. H.C. Fu, J.C. Huang, T.D. Wang, and C.C. Bampton: *Acta Mater.*, 1998, vol. 46, pp. 465-79.
22. I.C. Hsiao, S.W. Su, and J.C. Huang: *Metall. Mater. Trans. A*, 2000, vol. 31A, pp. 2169-80.
23. Y.N. Wang and J.C. Huang: *Mater. Chem. Phys.*, 2003, vol. 81, pp. 11-26.
24. G. Nussbaum, P. Sainfort, G. Regazzoni, and H. Gjestland: *Scripta Metall.*, 1989, vol. 23, pp. 1079-84.
25. H.K. Lin and J.C. Huang: *Mater. Trans.* 2002, vol. 43, pp. 2424-32.
26. Y.N. Wang, C.J. Lee, C.C. Huang, H.K. Lin, and J.C. Huang: *Mater. Sci. Forum*, 2003, vols. 426–432, pp. 2655-60.
27. C.L. Tsai and C.M. Tso: *ASM Metal Handbook*, ASM INTERNATIONAL, Materials Park, OH, 1993, vol. 6, pp. 12-13.
28. C.M. Adams: *Welding J.*, 1958, vol. 37 (5), pp. 210s-215s.
29. S. Kuo: *Welding Metallurgy*, John Wiley & Son, New York, NY, 1987, pp. 129-51.
30. B. Chalmers: *Principles of Solidification*, John Wiley & Sons, New York, NY, 1967.
31. L. Strezov and J. Herbertson: *Iron Steel Inst. Jpn. Int.*, 1998, vol. 38, pp. 959-65.